Research Article

Numerical Characterization of the Performance of Fluid Pumps Based on a Wankel Geometry

Stephen Wan, Jason Leong, Te Ba, Arthur Lim, and Chang Wei Kang

Institute of High Performance Computing, 1 Fusionopolis Way, No. 16-16 Connexis, Singapore 138632

Correspondence should be addressed to Stephen Wan; wansym@ihpc.a-star.edu.sg

The performance of fluid pumps based on Wankel-type geometry, taking the shape of a double-lobed limaçon, is characterized. To the authors' knowledge, this is the first time such an attempt has been made. To this end, numerous simulations for three different pump sizes were carried out and the results were understood in terms of the usual scaling coefficients. The results show that such pumps operate as low efficiency (<30%) valveless positive displacements pumps, with pump flow-rate noticeably falling at the onset of internal leakage. Also, for such pumps, the mechanical efficiency varies linearly with the head coefficient, and, within the onset of internal leakage, the capacity coefficient holds steady even across pump efficiency. Simulation of the flow field reveals a structure rich in three-dimensional vortices even in the laminar regime, including Taylor-like counterrotating vortex pairs, pointing towards the utility of these pumps in microfluidic applications. Given the planar geometry of such pumps, their applications as microreactors and micromixers are recommended.

1. Introduction

The present study is part of a larger effort aimed at exploring applications of fluid pumps based on Wankel-type geometry and is focused on the performance characterization of the simplest of such pumps.

Such Wankel-type pumps are essentially rotary positive displacement pumps, which operate by having an inner rotor orbit inside a chamber. The rotor path, determined by the chamber profile, creates a trapped fluid volume which is displaced through the chamber. In contrast to rotodynamic pumps, the trapped fluid is continually compressed to a high pressure without being imparted high kinetic energies. As a positive displacement pump, it has characteristics similar to the reciprocating positive displacement pump and, hence, would generate the same flow at a given speed (RPM) regardless of the discharge pressure, that is, a flat H-Q curve. However, a rotary pump is more susceptible to internal flow leakages especially at high pump heads, leading to a significant reduction in efficiency. The advantages of rotary pumps are that, as well as being able to deliver a flow that is less pulsatile compared with reciprocating piston pumps, they are more compact in design and capable of valveless operation.

There are a number of rotary pump types that have been well established and have found industrial application, such as the Gear Pump, Lobe Pump, Sliding-Vane Pump, Screw Pump, and Progressive-Cavity Pump [1], but so far, to the authors' knowledge, the Wankel-type design for fluid pump applications has not been exactly established. Although rarely reported, it is known that applications of fluid pumps based on Wankel-type geometry are not new. For example, Monties et al. [2] developed a valveless blood pump comprising a double-lobed limaçon-shaped chamber and an elliptically shaped rotor rotating on an eccentric gear. It had a single inlet and outlet and delivered pulsatile flow.

Mathematically, the perimeter of Wankel-type geometry is an epitrochoid, the parametric form of which is given by

$$x = e \cdot \cos(m\theta) + R\cos\theta, \tag{1a}$$

$$y = e \cdot \sin(m\theta) + R\sin\theta. \tag{1b}$$

In the case of the blood pump mentioned above and in the pumps examined in the present study, the pump chamber
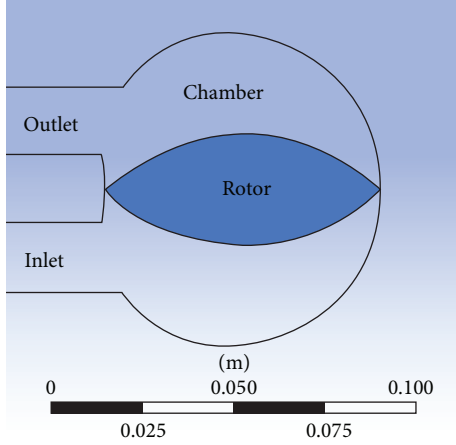
FIGURE 1: Estimated geometry of blood pump used in the calibration simulation.

geometry is obtained by setting $m = 2$ (see Figure 1), which is therefore the simplest of such geometries. (The well-known Wankel rotary engine chamber is generated by setting $m = 3$.)

In the present study, numerous computer simulations for three different pump sizes were carried out using commercially available computational fluid dynamics (CFD) codes (after calibrating a typical setup against experimental data). To the authors' knowledge, it appears that, to date, there has been no such previous attempt for these Wankel-type pumps, although there are numerous studies incorporating computational fluid dynamics (CFD) analyses, reported in the open literature, on particular and general aspects of various other pump types, including both rotodynamic and positive displacement pump types.

We list but several recent references, in the case of positive displacement type pumps, as follows. For gear pumps, see Riemslagh et al. [3] and Houzeaux and Codina [4]; for gerotor pumps, see Ruvalcaba and Hu [5]; for piston pumps, see Casoli et al. [6]; for progressive cavity pumps, see Paladino et al. [7]; for twin screw pumps, see Kovačević et al. [8]; and for vane pumps, see Takemori et al. [9].

In the case of rotodynamic pump types, for centrifugal pumps, see Gao et al. [10], Zhou et al. [11], Stel et al. [12], and Mihalić et al. [13]; for a mixed flow pump, see Liu et al. [14]; for a radial flow pump, see J.-H. Kim and K.-Y. Kim [15]; and for American Petroleum Institute (API) pumps, see Benigni et al. [16].

Numerical results generated in the present study were expressed in terms of the usual scaling coefficients. To conclude, we present details of the flow structure within the chamber for a pump sized for microfluidic applications.

2. Numerical Method

The simulations were carried out in a proprietary finite volume CFD code, ANSYS CFX v 15, using the immersed solid method to model the motion of the rotor.

2.1. Turbulence Model. To solve for the flow field, the shear-stress transport (SST) turbulence model of Menter [17]

was invoked to close the Reynolds averaged continuity and momentum equations (in standard Cartesian tensor notation):

$$\frac{\partial \rho}{\partial t} + \frac{\partial \left(\rho U_j \right)}{\partial x_j} = 0,$$

$$\frac{\partial \left(\rho U_i \right)}{\partial t} + \frac{\partial \left(\rho U_i U_j \right)}{\partial x_j} = -\frac{\partial P}{\partial x_i} + \frac{\left(\tau_{ij} - \rho \overline{u_i u_j} \right)}{\partial x_j} + S_M. \tag{2}$$

Details of the specific implementation of the SST model can be found in the ANSYS CFX manual [18]. Very briefly, the SST model calculates the Reynolds stresses, $-\rho \overline{u_i u_j} = \mu_t((\partial U_i/\partial x_j) + (\partial U_j/\partial x_i)) - (2/3)\rho k \delta_{ij}$, by solving a transport equation for the turbulent kinetic energy,

$$\frac{\partial \left(\rho k \right)}{\partial t} + \frac{\partial \left(\rho k u_i \right)}{\partial x_i} = \frac{\partial}{\partial x_j} \left(\Gamma_k \frac{\partial k}{\partial x_j} \right) + G_k - Y_k, \tag{3}$$

and another transport equation of the specific dissipation rate, ω, the ratio of energy dissipation rate, ε, to the turbulent kinetic energy, k:

$$\frac{\partial \left(\rho \omega \right)}{\partial t} + \frac{\partial \left(\rho \omega u_i \right)}{\partial x_i} = \frac{\partial}{\partial x_j} \left(\Gamma_\omega \frac{\partial \omega}{\partial x_j} \right) + G_\omega - Y_\omega + D_\omega. \tag{4}$$

The terms G_k and G_ω represent, respectively, the production of the turbulent kinetic energy, k, and the specific dissipation rate, ω, while the terms Y_k and Y_ω represent the dissipation of the turbulent kinetic energy, k, and the specific dissipation rate, ω. The cross-diffusion term, D_ω, arises from the transformation of the $k - \varepsilon$ model into the $k - \omega$ form. The effective diffusivities, $\Gamma_k = \mu + (\mu_t/\sigma_k)$ and $\Gamma_\omega = \mu + (\mu_t/\sigma_\omega)$, are obtained from turbulent Prandtl numbers for k and ω given by $\sigma_k = 1/(F_1/\sigma_{k,1} + (1 - F_1)/\sigma_{k,2})$ and $\sigma_\omega = 1/(F_1/\sigma_{\omega,1} + (1 - F_1)/\sigma_{\omega,2})$ (where F_1 is a blending function; and $\sigma_{k,1}, \sigma_{k,2}, \sigma_{\omega,1}$, and $\sigma_{\omega,2}$ are some constants). The value of the turbulent viscosity, μ_t, finally calculated from $\mu_t = a(\rho k/\omega)$, is limited by an expression, a, containing another blending function, F_2.

2.2. The Immersed Solid Technique. The immersed solid technique, implemented within the finite volume code of CFX [18], treats the presence of a solid object by applying a source term, S_M, to the momentum equation, in the fluid volume geometrically occupied by the solid object in the fluid domain. To track the movement of the immersed solid, the solver updates the mesh positions of the immersed solid at the beginning of each time step and applies the immersed solid sources, S_M, to the fluid nodes that lie within the immersed solid in an attempt to match the fluid velocity with the immersed solid velocity.

2.3. Simulation Calibration. The simulation setup for the pump performance characterization work was calibrated against the experimental data from [2, 19, 20]. To the authors' knowledge, it appears that, to date, these are the only sources of experimental data in the open literature for such pump types.
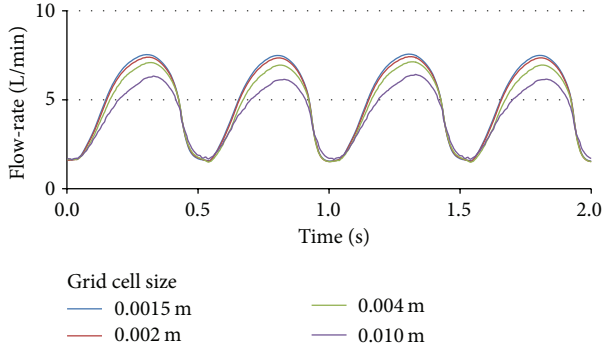
FIGURE 2: Instantaneous flow-rates obtained for various grid cell sizes in grid sensitivity study.
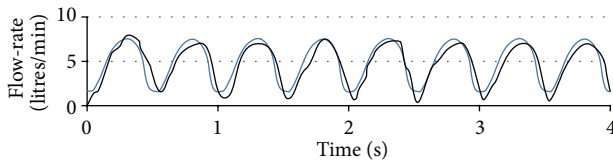

FIGURE 3: Predicted instantaneous flow-rate (blue curve) overlaid on experimental flow-rate (black line) from [1].

Direct comparison was not possible as the exact dimensions of the blood pump and fluid properties were not reported. By trial and error and by examination of the information available, the parameters of $R = 0.039$ m and $e = 0.0114$ m (which generated the size of the pump as shown in Figure 1) and a chamber thickness of 0.015 m were estimated.

A mesh grid sensitivity study was carried out by comparing instantaneous pump flow-rates obtained for different grid cell sizes. As shown in Figure 2, a cell size of 0.0015~0.0020 m would give reasonably accurate results. Using a time step of at least 1/500th of a period of shaft revolution and a mesh cell size of 0.002 m (yielding a total cell count of 55,000), we achieved reasonable agreement with the experimental data of Monties et al. [2], in terms of the instantaneous flow-rate time profile and magnitude, as indicated in Figure 3.

The uncertainty of the numerical results could not be assessed as Monties et al. [2] did not furnish information on the accuracy of and did not include error bounds on their experimental data. The mesh grids for the rotor and pump cavity for the calibration simulation are shown in Figure 4. A blood viscosity of 0.0035 Pa s and a density of $1.06E3$ kg/m^3 [21] were assumed. A first order upwind scheme was used to discretize the convective terms. Temporal discretization was performed with the first order backward Euler scheme performing 10 outward iterations per time step.

3. Pump Performance Scaling Studies

For the scaling studies, pumps of three different sizes of $R = 0.05$ m, $R = 0.1$ m, and $R = 0.2$ m were simulated and rotor tip clearances of $\Delta c = 0$ m (zero clearance), $\Delta c = 0.0025$ m, $\Delta c = 0.0064$ m, and $\Delta c = 0.0105$ m. Owing to the large

number of runs, 2D simulations were carried to complete the studies within a reasonable period of time.

Collected data were analyzed with the aid of the following dimensional groups: capacity coefficient, $C_Q = Q/NR^3$; head coefficient, $C_H = gH/N^2R^2$; efficiency, $\eta_P = \rho QgH/NT_R$; device Reynolds number, $Re = \rho NR^2/\mu$; and tip clearance ratio, $\epsilon = \Delta c/R$.

Time averaged values of flow-rate and reactive torque (over one cycle) were used in calculating the dimensional groups' values.

From the plots of capacity coefficient, C_Q, versus head coefficient, C_H, for various tip clearance ratios, ϵ, at a particular device Reynolds number, $Re = 1E6$ (Figure 5), we observe that the capacity coefficient, C_Q, remains constant up to a certain value of the head coefficient, C_H, beyond which it begins to drop noticeably, particularly for the largest tip clearance ratio, ϵ. These are typical of positive displacements pumps, where internal leakage would cause a deterioration of pump flow-rate at high pump heads. For a particular clearance ratio, we find that the pump efficiency varies fairly linearly with the head coefficient, C_H, across the three pump sizes studied here. See Figure 6.

It appears therefore that the capacity coefficient, C_Q, holds quite steady over variations in pump efficiency, η, as well. To confirm this, we ran simulations at a low and a higher efficiency and indeed the flow-rate, Q, scales linearly with NR^3 on a single line at these two disparate efficiencies ($\eta_P \sim 0.008$ and $\eta_P \sim 0.26$) as shown in Figure 7.

4. Pump Chamber 3D Flow Field

While the results of the above scaling studies are useful for a preliminary assessment of a suitable pump size for a particular application, detailed examination of the flow field in the pump chamber would be necessary to see if such pumps could be exploited for certain biomedical, microfluidic, or microreactor applications.

Hence, in this section, we report on a 3D simulation of pump scales to $R = 0.01$ m (which would be typical of an active microfluidic device) operating at a shaft speed of 200 rad/s on water against zero heads.

By plotting surface streamlines on a horizontal plane bisecting the thickness of the pump chamber as well as on a vertical plane along the axis of symmetry of the pump chamber for various rotor positions, as shown in Figure 8, it can already be observed that the flow pattern within the pump chamber is very complex.

Delving deeper, surface streamlines at various vertical planes across the pressure side of the pump chamber, for a particular rotor position, were then plotted. As shown in Figure 9, pairs of lateral vortices appear to first emerge near the tip of the rotor as indicated on plane P1. As the flow traverses the pump chamber, the vortices develop further while being stretched due to an increase in cross-sectional area in the main flow direction, from plane P2 to P5. By the time the flow reaches the outlet, the vortices appear to have more or less disappeared. A velocity vector plot on one of the planes, plane P2, as shown in Figure 10, clearly
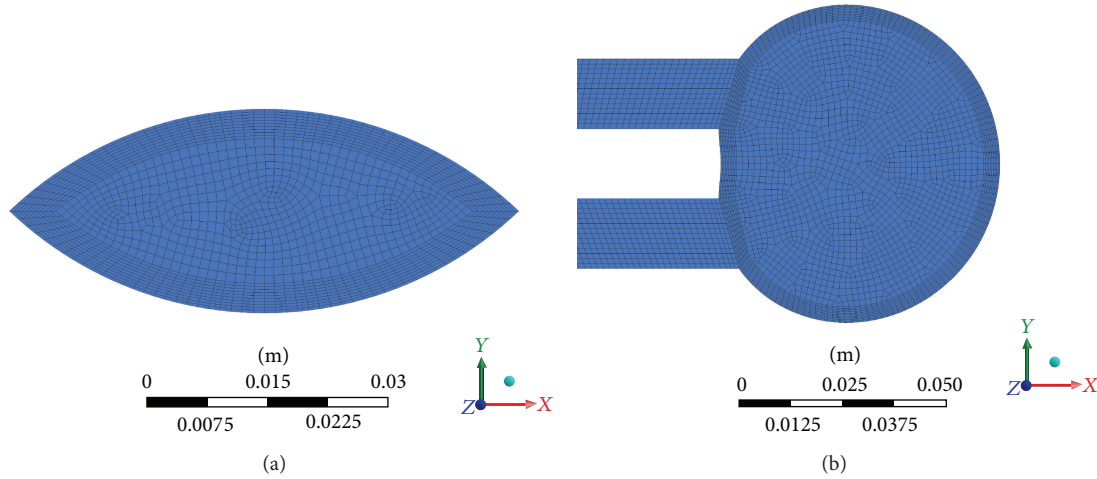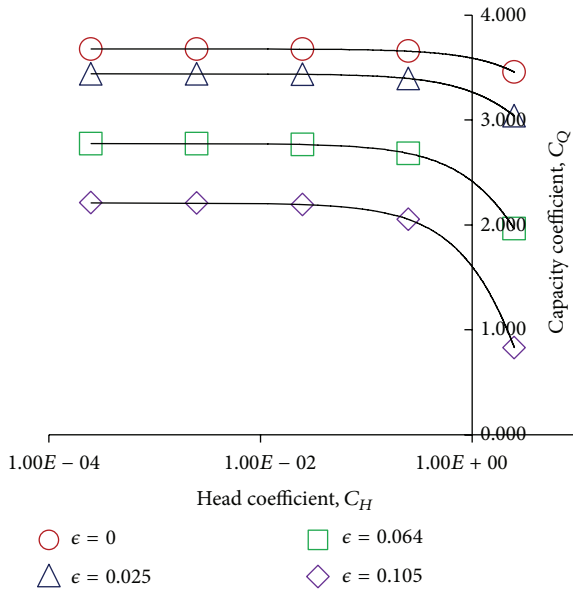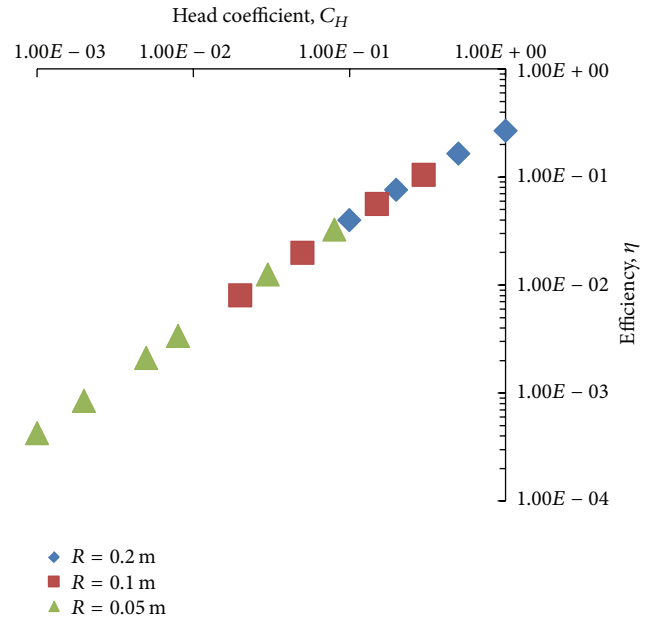
FIGURE 4: Mesh grid for the (a) rotor and (b) pump cavity.

FIGURE 5: Plots of capacity coefficient, C_Q, versus head coefficient, C_H, for various rotor tip clearance ratios, ϵ, for a particular device Reynolds number, Re = 1E6.

FIGURE 6: Variation of head coefficient, C_H, with pump efficiency, η_P, across three different pump sizes.

shows that these vortices resemble counterrotating Taylor vortices. The suction side of the pump chamber, on the other hand, is dominated by a lateral vortex in the horizontal plane (see again Figure 8). In essence, as the flow is drawn into the pump chamber, it sees a backward facing step, and the well-recognized recirculation zone is produced. A vector plot on a horizontal plane, as shown in Figure 11, confirms this observation.

Thus as the flow transits from the suction to the pressure sides, it is being continuously stretched from a pattern characterized by a dominant, horizontal lateral vortex to one characterized by pairs of vertical, lateral Taylor-like counterrotating vortices that are continuously deformed as the flow is being evacuated.

The resulting complex flow pattern, rich in three-dimensional vortices, suggests that pumps based on Wankel geometries have a good potential for mixing applications.

5. Concluding Remarks

We conclude this technical brief with the following salient points.

(i) A fluid pump based on the simplest Wankel geometry (double-lobed limaçon) operates as a positive displacement pump, without requiring the use of valves.
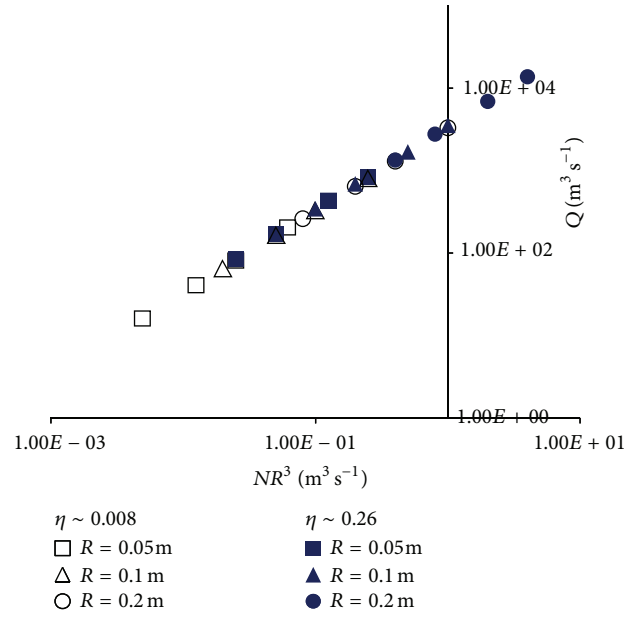
FIGURE 7: Linear scaling of pump flow-rate, Q, with NR^3 for two disparate pump efficiencies.
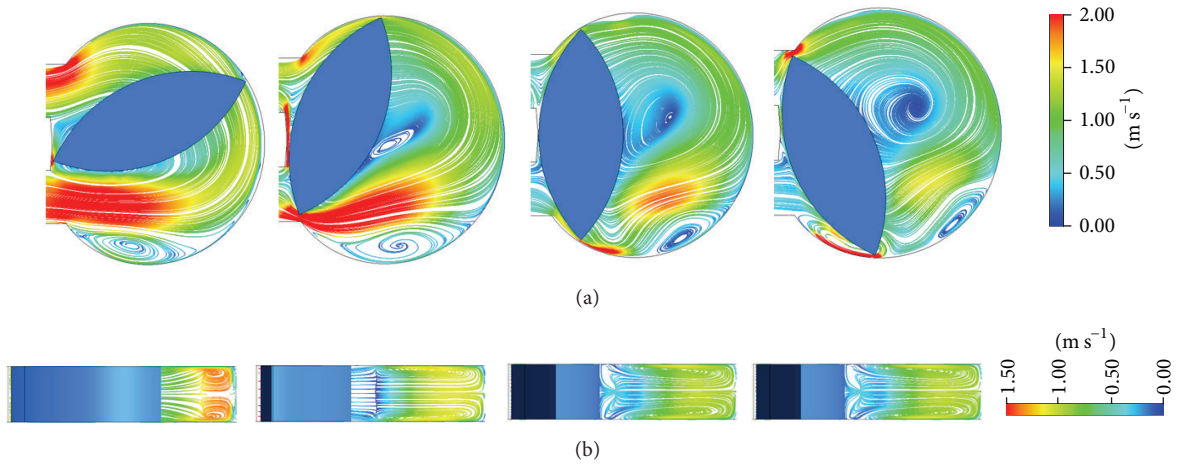

(a)

(b)

FIGURE 8: (a) Surface streamlines taken on a plane bisecting the thickness of the pump chamber for various rotor positions; (b) surface streamlines on a plane along the axis of symmetry of the pump chamber.
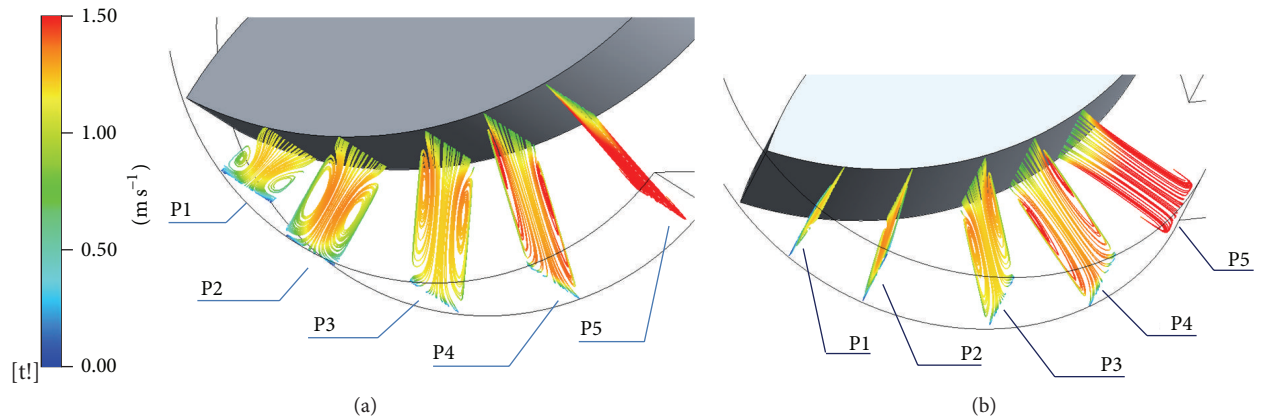

(a)

(b)

FIGURE 9: Two views of 2D streamlines on various cut-planes in the pressure side of the pump chamber, showing Taylor-like vortices being stretched as they traverse to the pump discharge.
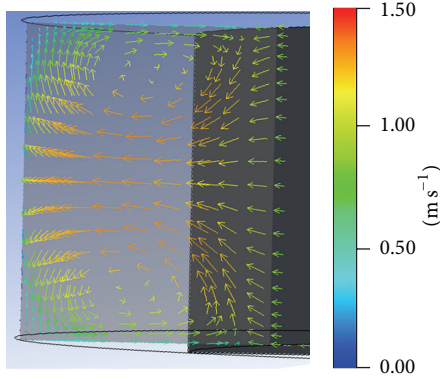
FIGURE 10: Velocity vectors plotted on one of the cut-planes in Figure 9, confirming the existence of Taylor-like counterrotating vortex pairs.
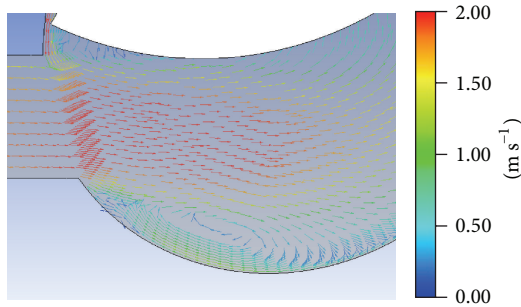

FIGURE 11: Velocity vectors plotted for one of the rotor positions in Figure 8, confirming a backward facing-type recirculation zone in the suction side of the pump.

(ii) As with positive displacement pumps in general, the capacity coefficient, C_Q, falls noticeably at the onset of fluid internal leakage.

(iii) For a particular set of dimensionless groups, pump efficiency, η_P, varies linearly with head coefficient, C_H.

(iv) Within the onset of internal leakage, the capacity coefficient, C_Q, holds steady even across pump efficiency, η_P, thus scaling pump flow-rate, Q, with shaft rotor speed, N, and the cube of rotor size, R (rotor centre-to-tip distance).

(v) Maximum pump efficiency is in the region of 30%.

(vi) Even in the laminar flow regime, flow structure within the pump chamber is complex and very rich in three-dimensional vortices.

(vii) Detailed examination of the flow structure reveals a transition from a structure dominated by a backward facing step type recirculation zone to one characterized by Taylor-like counterrotating vortex pairs that are continuously stretched, as the trapped fluid traverses from the suction side to the pressure side of the pump chamber.

(viii) It appears that a fluid pump based on the simplest Wankel geometry is best suited for applications in which pump efficiency is not an overriding issue; valveless operation is an advantage and complex flow patterns in the pump chamber are exploited to serve a particular function. Given the planar geometry of such pumps, their application as microreactors and micromixers is recommended.

Nomenclature

e: Epitrochoid eccentricity
g: Acceleration due to gravity
k: Turbulent kinetic energy
m: Epitrochoid shape parameter
C_H: Pump head coefficient
C_Q: Pump capacity coefficient
H: Pump head
N: Shaft speed
Q: Pump flow-rate
R: Rotor tip-to-centroid distance
Re: Device Reynolds number
S_M: Momentum source term
T_R: Reactive torque
ϵ: Ratio of rotor tip clearance to rotor tip-to-centroid distance
η_P: Pump mechanical efficiency
μ: Molecular viscosity
μ_T: Eddy viscosity
ρ: Fluid density
ω: Turbulent energy specific dissipation rate
Δc: Rotor tip clearance.

Conflict of Interests

The authors declare that there is no conflict of interests regarding the publication of this paper.

Acknowledgment

References

[1] K. Arnold and M. Stewarts, "Pumps," in *Surface Production Operations: Design of Oil-Handling System and Facilities*, vol. 1, pp. 333–354, 1999.

[2] J. R. Monties, P. Havlik, T. Mesana, J. Trinkl, J. L. Tourres, and J. L. Demunck, "Development of the Marseilles pulsatile rotary blood pump for permanent implantable left ventricular assistance," *Artificial Organs*, vol. 18, no. 7, pp. 506–511, 1994.

[3] K. Riemslagh, J. Vierendeels, and E. Dick, "An arbitrary Lagrangian-Eulerian finite-volume method for the simulation of rotary displacement pump flow," *Applied Numerical Mathematics*, vol. 32, no. 4, pp. 419–433, 2000.

[4] G. Houzeaux and R. Codina, "A finite element method for the solution of rotary pumps," *Computers and Fluids*, vol. 36, no. 4, pp. 667–679, 2007.

[5] M. A. Ruvalcaba and X. Hu, "Gerotor fuel pump performance and leakage study," in *Proceedings of the ASME International Mechanical Engineering Congress & Exposition*, pp. 807–815, Denver, Colo, USA, November 2011.

[6] P. Casoli, A. Vacca, G. Franzoni, and G. L. Berta, "Modelling of fluid properties in hydraulic positive displacement machines," *Simulation Modelling Practice and Theory*, vol. 14, no. 8, pp. 1059–1072, 2006.

[7] E. E. Paladino, J. A. Lima, P. A. S. Pessoa, and R. F. C. Almeida, "A computational model for the flow within rigid stator progressing cavity pumps," *Journal of Petroleum Science and Engineering*, vol. 78, no. 1, pp. 178–192, 2011.

[8] A. Kovačević, N. Stošić, and I. K. Smith, "Numerical simulation of combined screw compressor-expander machines for use in high pressure refrigeration systems," *Simulation Modelling Practice and Theory*, vol. 14, no. 8, pp. 1143–1154, 2006.

[9] C. K. Takemori, E. E. Paladino, and L. Lessa, "Numerical simulation of oil flow in a power steering pump," SAE Technical Paper 2005-01-4061, SAE, 2005.

[10] Z. Gao, W. Zhu, L. Lu, J. Deng, J. Zhang, and F. Wuang, "Numerical and experimental study of unsteady flow in a large centrifugal pump with stay vanes," *Journal of Fluids Engineering, Transactions of the ASME*, vol. 136, no. 7, Article ID 071101, 2014.

[11] L. Zhou, W. Shi, W. Li, and R. Agarwal, "Numerical and experimental study of axial force and hydraulic performance in a deep-well centrifugal pump with different impeller rear shroud radius," *Journal of Fluids Engineering*, vol. 135, no. 10, Article ID 104501, 2013.

[12] H. Stel, G. D. L. Amaral, C. O. R. Negrão, S. Chiva, V. Estevam, and R. E. M. Morales, "Numerical analysis of the fluid flow in the first stage of a two-stage centrifugal pump with a vaned diffuser," *Journal of Fluids Engineering*, vol. 135, no. 7, Article ID 071104, 2013.

[13] T. Mihalić, Z. Guzović, and A. Predin, "Performances and flow analysis in the centrifugal vortex pump," *Journal of Fluids Engineering*, vol. 135, no. 1, Article ID 011002, 2013.

[14] J. Liu, Z. Li, L. Wang, and L. Jiao, "Numerical simulation of the transient flow in a radial flow pump during stopping period," *Journal of Fluids Engineering, Transactions of the ASME*, vol. 133, no. 11, Article ID 111101, 7 pages, 2011.

[15] J.-H. Kim and K.-Y. Kim, "Analysis and optimization of a vaned diffuser in a mixed flow pump to improve hydrodynamic performance," *Journal of Fluids Engineering*, vol. 134, no. 7, Article ID 71104, 2012.

[16] H. Benigni, H. Jaberg, H. Yeung, T. Salisbury, O. Berry, and T. Collins, "Numerical simulation of low specific speed American petroleum institute pumps in part-load operation and comparison with test rig results," *Journal of Fluids Engineering*, vol. 134, no. 2, Article ID 024501, 2012.

[17] F. R. Menter, "Two-equation eddy-viscosity turbulence models for engineering applications," *AIAA Journal*, vol. 32, no. 8, pp. 1598–1605, 1994.

[18] ANSYS, *CFX User's Manual, Version 5*, ANSYS, Cecil Township, Pa, USA, 2014.

[19] J.-R. E. Monties, J. Trinkl, T. Mesana, P. J. Havlik, and J.-L. Y. Demunck, "Cora valveless pulsatile rotary pump: new design and control," *Annals of Thoracic Surgery*, vol. 61, no. 1, pp. 463–468, 1996.

[20] T. Mesana, S. Morita, J. Trinkl et al., "Experimental use of a semipulsatile rotary blood pump for cardiopulmonary bypass," *Artificial Organs*, vol. 19, no. 7, pp. 734–738, 1995.

[21] "The Physics Hypertextbook," http://physics.info/.